Generating Mock Catalogs for the Baryon Oscillation Spectroscopic Survey: An Approximate N-Body approach

Tomomi Sunayama[a], Nikhil Padmanabhan[a], Katrin Heitmann[b], Salman Habib[b], Steve Rangel[b,c]

[a]Yale University, New Haven, CT
[b] Argonne National Laboratory, Lemont, IL
[c] Northwestern University, Evanston, IL

E-mail: tomomi.sunayama@yale.edu, nikhil.padmanabhan@yale.edu,heitmann@anl.gov, habib@anl.gov,steverangel@u.northwestern.edu

Abstract. Precision measurements of the large scale structure of the Universe require large numbers of high fidelity mock catalogs to accurately assess, and account for, the presence of systematic effects. We introduce and test a scheme for generating mock catalogs rapidly using suitably derated N-body simulations. Our aim is to reproduce the large scale structure and the gross properties of dark matter halos with high accuracy, while sacrificing the details of the halo's internal structure. By adjusting global and local time-steps in an N-body code, we demonstrate recovery of the relevant large scale probes, including individual halo masses, to better than 2% and the power spectrum to $k = 1h\mathrm{Mpc}^{-1}$, to better than 1%, while requiring a factor of 4 less CPU time. To reduce the number of output snapshots, we also test the redshift spacing of outputs required to generate simulated light cones. We find that outputs separated by $\Delta 0.05$ allow us to interpolate particle positions and velocities with sufficient accuracy to reproduce the real and redshift space power spectra to better than 1% (out to $k = 1h\mathrm{Mpc}^{-1}$). Even with a redshift spacing as large as $\Delta z = 0.25$, these errors only degrade to less than 2% in both real and redshift space. As a practical demonstration of these ideas, we generate a suit of simulations matched to the Baryon Oscillation Spectroscopic Survey (BOSS).

Keywords: cosmology; large-scale structure of Universe, cosmological parameters, galaxies; halos, statistics

Contents

1 Introduction

Large-volume spectroscopic surveys of the Universe (CITE SDSS, WiggleZ, BOSS) are revolutionizing our understanding of cosmology and structure formation. Based on these successes, a new generation of surveys (CITE DESI, Euclid, WFIRST) is being planned that will improve our constraints by an order of magnitude (or more). This unprecedented improvement in statistical precision places stringent demands on the theoretical modeling and analysis techniques; simulations will play an essential in meeting these requirements.

One of the challenges for simulations are the varied roles they play, and the different requirements these impose on the simulations. At one extreme, simulations are necessary for generating sample covariances for the data and measurements. This typically requires very large volumes to simulate entire surveys thousands of times, but have lower accuracy requirements. Motivated by these considerations, a number of recent studies have investigated methods designed to produce mock catalogs with reduced accuracy, but much higher throughput compared to the full N-body simulations [? ? ? ? ? ? ? ? ? ? ?]. An open question still is the effect of changing the input cosmology used to generate the covariance matrix on cosmological inferences, and how best to implement such variations. More recently, the impact of super-survey modes (modes outside the survey volume) on inferred errors has been shown to be potentially larger than previously appreciated (CITES??) and is an area of active study.

At the other extreme, simulations are crucial for calibrating the theoretical models used to fit the data. Examples here are quantifying shifts in the baryon acoustic oscillation distance scale due to nonlinear evolution and galaxy bias (CITES), or templates used to fit the full shape of the correlation function. For such applications, one ideally requires high fidelity simulations. The volume requirements are significantly reduced from that for covariance matrices, but still need to much larger than survey volumes to keep systematic errors below statistical errors.

An intermediate application are the generation of mock catalogs that capture the observational characteristics of surveys (eg. geometry, selection effects). The importance of these cannot be underestimated, since the effects of many observational systematics can only be quantitatively estimated by simulating them. These issues will get progressively more important for the next generations of surveys which will move away from highly complete and pure samples that have mostly been used for cosmological studies to date.

The simplest way to generate approximate density fields is to use analytic approximations such as Lagrangian perturbation theory followed by prescriptions to put in halos in a way that better matches results from N-body simulations [? ?], or simply to run lower resolution N-body codes with a small number of time-steps [?], or a combination of the two approaches [?]. These methods are successful in capturing the large-scale density field but lose information at small scales. Because of their speed, they can be used to produce large numbers of simulations required to build sample covariance matrices, at error levels ranging from $5 - 10\%$ (depending on the quantities being predicted). It is difficult to estimate, however, what the loss of accuracy implies for tests of systematic errors, which may need to be modeled at the $\sim 1\%$ level.

The approach we take here is to reduce the small-scale accuracy of a high-resolution N-body code by coarsening its temporal resolution. In the present case, the time-stepping consists of two components, (i) a long time step for solving for evolution under the long-range particle-mesh (PM) force, and (ii) a set of underlying sub-cycled time steps for a short-range particle-particle interaction, computed either via a tree-based algorithm, or by direct particle-particle force evaluations. The idea is to reduce the number of both types of time steps while preserving enough accuracy to correctly describe the large scale distribution of galaxies, as modeled by a halo occupation distribution (HOD) approach. Our first goal in this paper is, therefore, to quantitatively understand the impact of the

temporal resolution on the halo density field and how best to accurately reproduce the details of the halo density field on large scales, sacrificing small scale structure information. This allows to generate a suite of large volume simulations, spanning a range of cosmologies. This paper presents the details of these simulations and outlines future applications.

This paper is organized as follows. Sec. 2 briefly describes the Hardware/Hybrid Accelerated Cosmology Code (HACC) N-body framework we use to generate our simulations, focusing on the flexibility in the time-stepping that we exploit here. Sec. 3 presents a sequence of convergence tests where we evaluate the effects of time-stepping on the halo density field. Sec. 4 discusses interpolating between saved time steps, necessary for constructing light-cone outputs. Sec. 5 presents an example application of these simulations : generating mock catalogs that match the BOSS galaxy sample. (NOTE : Can we put in another simple application?) We conclude in Sec. 6 by outlining possible future directions.

All simulations and calculations in this paper assume a ΛCDM cosmology with $\Omega_m = 0.2648$, $\Omega_\Lambda = 0.7352$, $\Omega_b h^2 = 0.02258$, $n_s = 0.963$, $\sigma_8 = 0.8$ and $h = 0.71$.

2 HACC

All simulations in this paper were carried out using the HACC (Hardware/Hybrid Accelerated Cosmology Code) framework. HACC provides an advanced, architecture-agile, extreme-scale N-body capability targeted to cosmological simulations. It is descended from an approach originally developed for the heterogeneous architecture of Roadrunner [? ?], the first computer to break the petaflop performance barrier.

HACC's flexible code architecture combines MPI with a variety of more local programming models, (e.g., OpenCL, OpenMP) and is easily adaptable to different platforms. HACC has demonstrated scaling on the entire IBM BG/Q Sequoia system up to 1,572,864 cores with an equal number of MPI ranks, attaining 13.94 PFlops at 69.2% of peak and 90% parallel efficiency (for details, see Ref.[?]). Examples of science results obtained using HACC include 64-billion particle runs for baryon acoustic oscillations predictions for the BOSS Lyman-α forest [?], high-statistics predictions for the halo profiles of massive clusters [?], and 0.5 and 1.1 trillion particle runs at high mass resolution. A recent overview of the HACC framework can be found in Ref. [?].

HACC uses a hybrid parallel algorithmic structure, splitting the force calculation into a specially designed grid-based long/medium range spectral PM component that is common to all computer architectures, and an architecture-specific short-range solver. Modular code design combined with particle caching allows the short-range solvers to be 'hot-swappable' on-node; they are blind to the parallel implementation of the long-range solver. The short-range solvers can use direct particle-particle interactions, i.e., a P^3M algorithm [?], as on (Cell or GPU) accelerated systems, or use tree methods on conventional or many-core architectures. (This was the case for the simulations reported here.) In all cases, the time-stepping scheme is based on a symplectic method with (adaptive) sub-cycling of the short-range force. The availability of multiple algorithms within the HACC framework allows us to carry out careful error analyses, for example, the P^3M and the TreePM versions agree to within 0.1% for the nonlinear power spectrum test in the code comparison suite of Ref. [?].

As already discussed, an important feature of the work presented here is the ability to carry out error-controlled approximate simulations at high throughput. In order to understand how we implement this, some details of the HACC time-stepping algorithm are now provided. Evolution is viewed as a symplectic map on phase space: $\zeta(t) = \exp(-t\mathbf{H})\zeta(0)$ where, ζ is a phase-space vector $(\mathbf{x}, \mathbf{v})$, H is the (self-consistent) Hamiltonian, and the operator, $\mathbf{H} = [H,\ ]_P$, denotes the action of taking the Poisson bracket with the Hamiltonian. Suppose that the Hamiltonian can be written as the sum of two parts; then by using the Campbell-Baker-Hausdorff (CBH) series we can build an integrator for the time evolution; repeated application of the CBH formula yields

$$\exp(-t(\mathbf{H}_1 + \mathbf{H}_2)) = \exp(-(t/2)\mathbf{H}_1)\exp(-t\mathbf{H}_2)\exp(-(t/2)\mathbf{H}_1) + O(t^3),$$

a second order symplectic integrator. In the basic PM application, the Hamiltonian H_1 is the free particle (kinetic) piece while H_2 is the one-particle effective potential; corresponding respectively

to the 'stream' and 'kick' maps $M_1 = \exp(-t\mathbf{H}_1)$ and $M_2 = \exp(-t\mathbf{H}_2)$. In the stream map, the particle position is drifted using its known velocity, which remains unchanged; in the kick map, the velocity is updated using the force evaluation, while the position remains unchanged. This symmetric 'split-operator' step is termed SKS (stream-kick-stream). A KSK scheme constitutes an alternative second-order symplectic integrator.

In the presence of both short and long-range forces, we split the Hamiltonian into two parts, $H_1 = H_{sr} + H_{lr}$ where H_{sr} contains the kinetic and particle-particle force interaction (with an associated map M_{sr}), whereas, $H_2 = H_{lr}$ is just the long range force, corresponding to the map M_{lr}. Since the long range force varies relatively slowly, we construct a single time-step map by sub-cycling M_{sr}: $M_{full}(t) = M_{lr}(t/2)(M_{sr}(t/n_c))^{n_c}M_{lr}(t/2)$, the total map being a usual second-order symplectic integrator. This corresponds to a KSK step, where the S is not an exact stream step, but has enough M_{sr} steps composed together to obtain the required accuracy. (We take care that the time-dependence in the self-consistent potential is treated correctly; HACC uses the scale factor, a, as the time variable.) As discussed later below, we will use the flexibility in the sub-cycling as a way of reducing the number of time steps such that the loss of accuracy only affects the resolution at very small scales, which, as discussed previously, are not of interest in the current set of simulations.

3   Time Step Tuning

In this section, we systematically examine how reducing the number of time steps affects individual halo properties (i.e., halo masses, positions, and velocities), as well as aggregate statistics like the mass function and spatial clustering. We run a set of convergence tests with boxes of size $(256h^{-1}\mathrm{Mpc})^3$ with 256^3 particles. These runs have the same particle mass as the main $(4000h^{-1}\mathrm{Mpc})^3$ volume simulations. We run these with the following time step options : 450/5, 300/3, 300/2, 150/3 and 150/2 where the first number is the number of long time-steps, while the second is the number of subcycles. The 450/5 case has been independently verified to give fully converged results and is the baseline against which we compare all other results. Each simulation is started from the same initial conditions and evolved down to $z = 0.15$. We demonstrate that the 300/2 case, corresponding to $\Delta a \approx 0.003$ reproduces the full resolution simulation for all the large scale properties we consider, and is our choice for the mocks presented in Sec. 5.

3.1   Matching

In order to compare detailed halo properties we need to match individual halos across different runs (reference vs. run under test). We first discuss the algorithm used for identifying the corresponding halos in the two cases and then compare halo mass, position, and velocity for the matched halos. From this quantitative comparison, we find that the simulations with 300 global time steps have significantly less scatter in the measured quantities, compared to the baseline determined by the 450/5 simulation, than do the samples with 150 global steps. In addition, we find that the differences between the different sub-cycling choices are almost negligible.

3.1.1   Algorithm

All simulations share the same particle initial conditions, allowing us to match halos in different runs by matching their individual particle content. Given a halo in simulation A, we consider all halos in simulation B that between them hold all the particles belonging to the halo in simulation A. Given this list of possible matches, we choose the run B halo with the largest number of common particles with the reference halo in run A. To avoid spurious matches, we also require that the fraction of common particles (relative to simulation A) exceeds a given threshold. To illustrate how this matching algorithm works, we use the samples from the 300/2 simulation and the 450/5 simulation, and adopt a threshold of 50% as our default choice. (Figure **??** demonstrates that the unmatched fraction increases with increasing threshold and decreasing halo mass.)
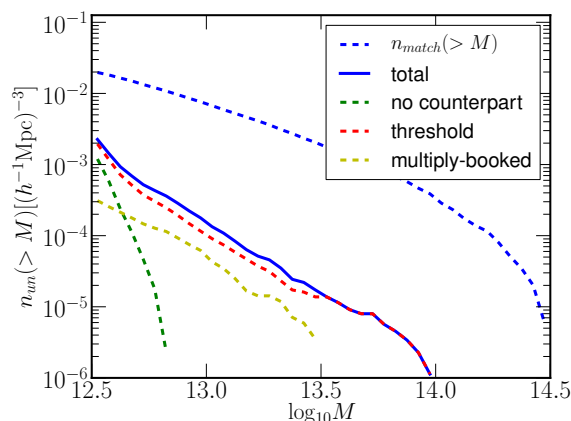
Figure 1. Itemization of unmatched halos (from the 450/5 and 300/2 simulations at $z = 0.15$) shown as cumulative number densities of the unmatched halos arising from each procedure in the matching algorithm. The solid blue line is the total number density of the unmatched halos. The dashed green line shows halos with no counterpart – none of the particles were identified as belonging to a halo in the comparison simulation; this is significant only at low halo mass. The dashed red line shows halos eliminated because of not meeting the matching threshold (i.e., the halos do not have enough of a fraction of the same particles). The dashed cyan line is for the halos eliminated because multiple halos correspond to one halo (see text).

The matching algorithm described above is unidirectional, hence multiple halos in run A may have particles resident in a single halo in run B; in our simulations, this happens at the 1-2% level, adopting a particle matching threshold of 50%. We refer to these cases as 'multiply-booked' halos. Figure **??** compares halo masses matching the 450/5 simulation to the 300/2 simulation for the case of multiply-booked halos, as well as the rest. The top left panel shows the mass scatter for all the matched halos between the two simulations, while the top right panel shows the mass scatter only for the non multiply-booked halos. The bottom panels show the mass scatter for the case of multiply-booked halos only. The bottom left panel shows the mass scatter for individual multiply-booked halos, while the bottom right panel plots the summed halo mass for the corresponding halos. The overall behavior represented in Figure **??** is straightforward to interpret.

As the top left panel shows, there are low-mass halos in the 450/5 simulation corresponding to high-mass halos in the 300/2 simulation. The same trend is observed for the case of multiply-booked halos (bottom left panel), but not for the non-multiply-booked halos (top right). Furthermore, the disagreement for halo masses between the two simulations are resolved by adding the corresponding halo masses. This implies that there are multiple halos in the 450/5 simulation which are merged into one halo in the 300/2 simulation. The smaller number of time steps in the 300/2 simulations reduces substructure as well as the compactness of the halos compared to the 450/5 simulation. Thus, for a small fraction of halos in the 450/5 simulation, individual halos can be merged into a single halo in the 300/2 simulation.

Figure **??** shows the number densities of the unmatched halos in the 450/5 simulation when compared to the 300/2 simulation at $z = 0.15$. There are three reasons that halos can turn up as unmatched. In the first case, particles forming a halo in simulation A may not form a component of a halo in simulation B (no common particles). Second, if the fraction of common particles over the total number of particles in each halo is less than the threshold of 50%, these halos will be eliminated from the matching set. Finally, for the case of multiply-booked halos, we remove all but the one with the largest number of common particles. In Figure **??**, we show each type of unmatched number density as a function of halo mass. The first case occurs only for low halo masses, where low effective resolution in a simulation can lead to halo drop out (halos are too 'fuzzy' to meet the FOF overdensity criterion), and falls off steeply with rising halo mass. Most of the unmatched halos arise due to their not passing the threshold criterion. The loss of matching due to multiple-booking follows the trend of the below-threshold case, but at a reduced level. We have checked that the trends discussed here
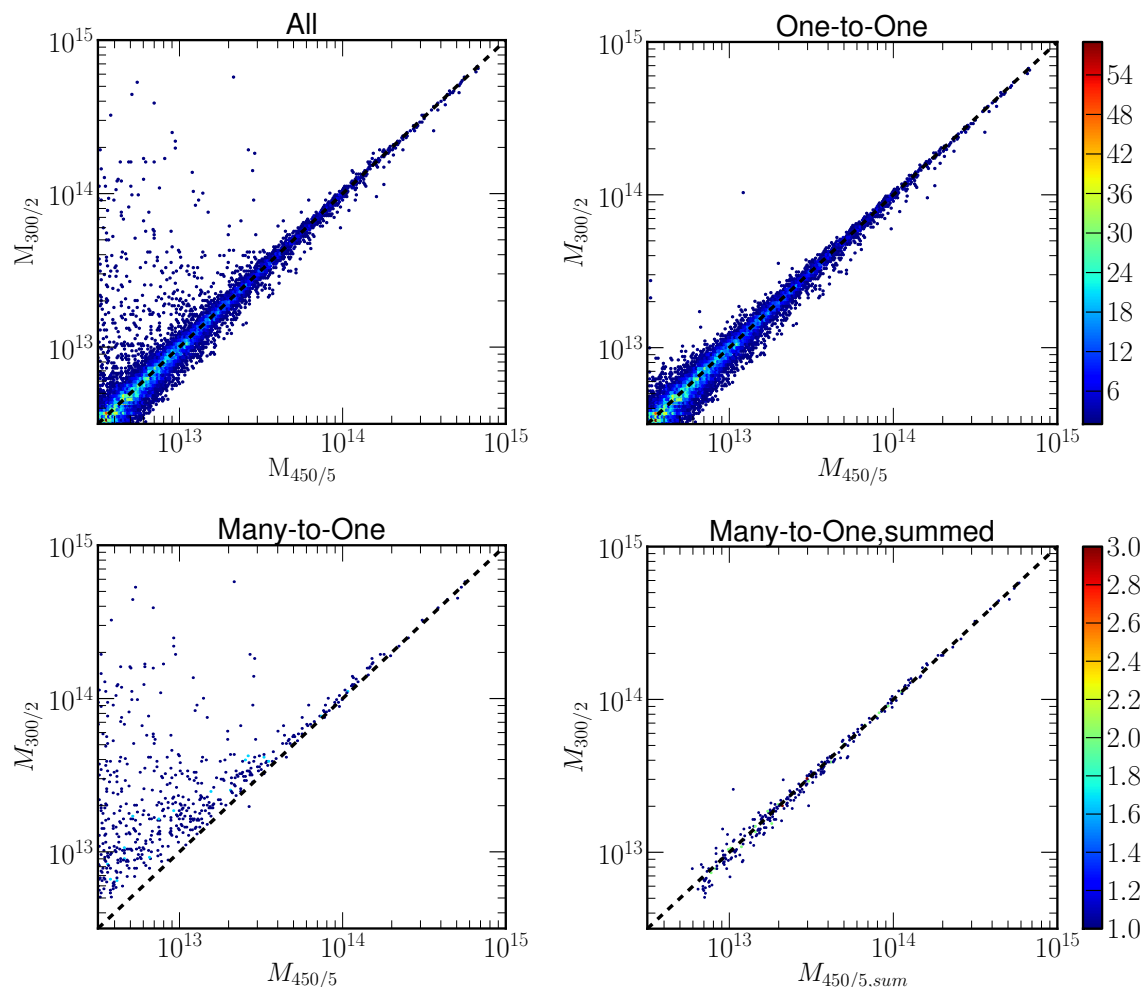
Figure 2. Distribution of halo masses comparing matched halos in the 450/5 simulation (x-axis) to the 300/2 simulation (y-axis) at $z = 0.15$. Panels correspond to halos with different matching criteria imposed: all the matched halos (top left), the vast majority of matched halos having one-to-one correspondence (top right), matched halos not having one-to-one correspondence called "multiply-booked" halos (bottom left), and the multiply-booked halos whose corresponding halo masses are added (bottom right). The results shown in these panels imply that the low-mass scatter between the 450/5 simulation and the 300/2 simulation shown in the top left panel arises when "multiply-booked" halos in the 450/5 simulation are merged into one halo in the 300/2 simulation due to an effectively worse resolution in this case.

are not affected by redshift.

3.1.2 Halo Properties

We now systematically compare halo properties (i.e., halo mass, position, and velocity) for halos in the lower resolution runs that were successfully matched to those in the 450/5 simulation. We are interested in correctly describing the large-scale distribution of galaxies using an HOD approach; this requires that only the dark matter halo locations and masses be estimated sufficiently accurately.

The comparison of halo mass for different time-stepping schemes to the 450/5 simulation at $z = 0.15$ is shown in Figure **??**. We take all the matched halos whose masses are between $10^{12.5} \mathrm{M}_\odot$ to $10^{13.0} \mathrm{M}_\odot$, $10^{13.0} \mathrm{M}_\odot$ to $10^{13.5} \mathrm{M}_\odot$, and $10^{13.5} \mathrm{M}_\odot$ to $10^{14.0} \mathrm{M}_\odot$, and compute their means and standard deviations for $\log_{10}(\mathrm{M}/\mathrm{M}_{450/5})$, where $M_{450/5}$ is a halo mass for the 450/5 simulation and M corresponds to a halo in the samples generated with different time-stepping schemes. Figure **??** shows

that halos generated from the simulations with small number of time steps have systematically lower FOF masses than those in the 450/5 simulation. (The same linking length ($b = 0.168$) is used in the FOF algorithm to define halos for all the simulations.) Under these circumstances, the FOF mass is highest in the 450/5 simulation, decreasing systematically with increase in loss of temporal resolution.

NOTE: because FOF masses come from particles within an isodensity contour, it is not obvious that making the resolution worse will actually reduce the mass – it can even increase the mass, depending on the circumstances (see Bhattacharya et al. arXiv:1005.2239, the Appendix)
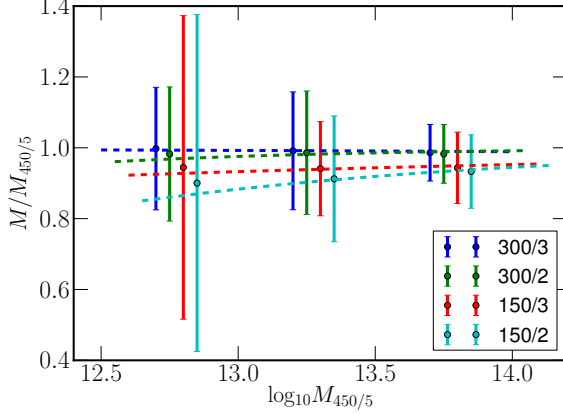
Figure 3. Comparison of halo mass (FOF, $b = 0.168$) for matched halos between the 450/5 simulation and coarsened time-stepping schemes at $z = 0.15$. We take all the matched halos whose masses are between $10^{12.5}M_\odot$ to $10^{13.0}M_\odot$, $10^{13.0}M_\odot$ to $10^{13.5}M_\odot$, and $10^{13.5}M_\odot$ to $10^{14.0}M_\odot$, and compute the mean and the standard deviation for $\log_{10}(M/M_{450/5})$ where $M_{450/5}$ is a halo mass for the 450/5 simulation and M is for the simulations with different number of time steps corresponding to different colors in the plot. The x-positions have been displaced to avoid overlapping the error bars. Halo masses decrease systematically as the time resolution is coarsened.

Figure **??** shows the differences in positions (left panel) and velocities (right panel) for the matched halos at $z = 0.15$. Simulations with a smaller number of global time steps (150) display significantly more scatter; they also show a small bias in the speed. With 300 global time steps, the results are much improved; the velocity bias is almost entirely removed and the scatter is significantly reduced. The standard deviation in the differences in halo distances is matched is better than $200h^{-1}$kpc in these cases. The distributions are very close to Gaussian. As is clear from Figure **??**, the difference between 3 and 2 sub-cycles is insignificant for our purposes. We observe the same trend in halo properties discussed here at different redshifts.

As shown in Figure **??**, the fraction of unmatched halos in the 300/2 simulation to the 450/5 simulation is less than 5% on most of halo mass ranges, which implies that the 300/2 simulation has almost the same number of halos as in the 450/5 simulation. Furthermore, Figure **??** shows that the halo masses in the 450/5 and 300/2 simulations have linear relation with the slope being one. So, most of halos in the 300/2 simulation have the same mass as the ones in the 450/5 simulation. Since the number of sub-cycles do not affect to halo positions and velocities as shown in Figure **??**, the 300/2 time step is our choice to save the simulation time while keeping the halo properties almost identical to the 450/5 simulation.

The results shown in Figures **??**, **??**, and **??**, show that the the 300/2 option has a low ratio of unmatched halos (less than 5%), excellent halo mass correlation to the 450/5 simulation (the small mass bias can be easily corrected as described below), and sufficiently small scatter in halo position. This time-stepping option is therefore a good candidate for generating mock catalogs efficiently, while maintaining high accuracies. In terms of the time savings alone, this will result in an increased capacity to generate high quality catalogs by a factor of four, which is quite significant. We will consider memory and storage savings further below in Section 4.
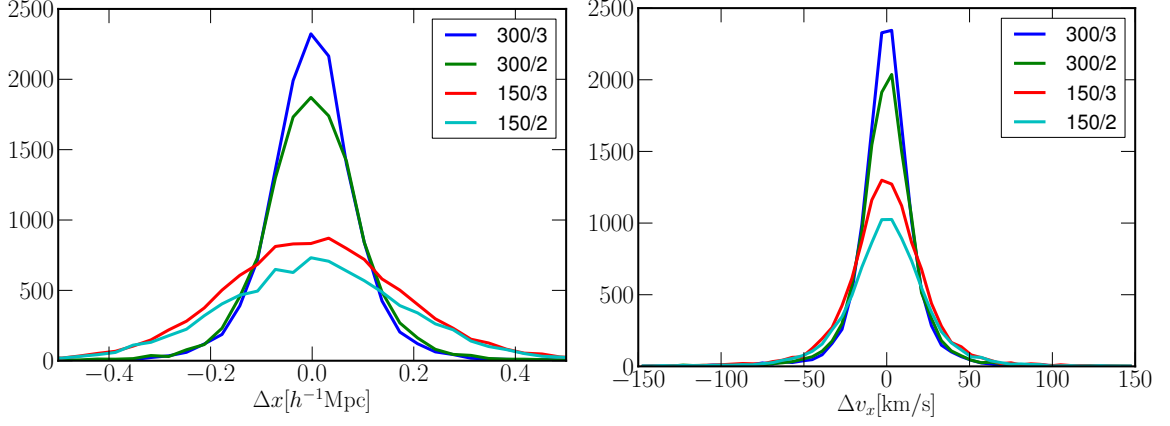
Figure 4. Comparison of the positions (left) and velocities (right) of halos matched across simulations with different time steps. The reference simulation is 450/5 while the colors correspond to 300/3 (blue), 300/2 (green), 150/3 (red), and 150/2 (cyan). The dashed lines are Gaussian fits.

	α	β
300/3	0.005	0.175
300/2	0.07	-0.47
150/3	0.101	-0.162
150/2	0.315	-0.411

Table 1. Mass reassignment parameters α and β of Eq. **??** for simulations run with different numbers of time steps (the results are shown at $z = 0.15$).

3.1.3 Halo Mass Adjustment and Resulting Observables

Halos generated by the de-tuned simulations have systematically lower masses than the halos in the 450/5 simulation as shown in Figure **??**. In the following, we describe how to implement a systematic mass correction by matching to the 450/5 results; we also display the resulting observables including mass functions and power spectra.

To undertake the mass calibration, we first take all the matched halos between the 450/5 simulation and the de-tuned simulations and compute means for each mass bin. We consider only the matched halos because the aim of the mass adjustment is to correct systematic mass differences for the halos that are theoretically identical in the different runs. After computing the means for each mass bin, we fit them to a functional form that brings the reassigned halo mass, M_{re}, close to the average halo mass for the 450/5 simulation. For our simulations, we find that the following simple form suffices for this task:

$$M_{re} = M(1.0 + \alpha(M/10^{12.0}[\mathrm{M_\odot}])^\beta, \tag{3.1}$$

where M_{re} is the reassigned halo mass, M is the original halo mass, and α and β are free parameters. The α and β values for the simulations with different numbers of time steps are listed in Table **??** (at $z = 0.15$). The best-fit parameters α and β are functions of redshift. For the case of the 300/2 simulation, the best fit parameters are $\alpha(z) = 0.123z + 0.052$ and $\beta(z) = -0.154z - 0.447$.

Given the mass corrections, we now compute mass functions using the results from the different time-stepping schemes, as shown in Figure **??**, where we use the 450/5 simulation at $z = 0.15$ as the reference. In Figure **??**, we show the ratio $n(> M)/n_{450/5}(> M)$, where $n_{450/5}(> M)$ is a cumulative mass function for the 450/5 simulation and $n(> M)$ is a cumulative mass function for the other cases. We compare the results before and after mass adjustment. While the mass functions from the 250/3 and 150/2 simulations are suppressed by more than 10% on all mass ranges before correction, they are

significantly improved afterwards, especially for halo masses greater than $10^{13.0} M_\odot$. For simulations with 300 global time steps, the mass adjustment is especially effective at small halo masses.
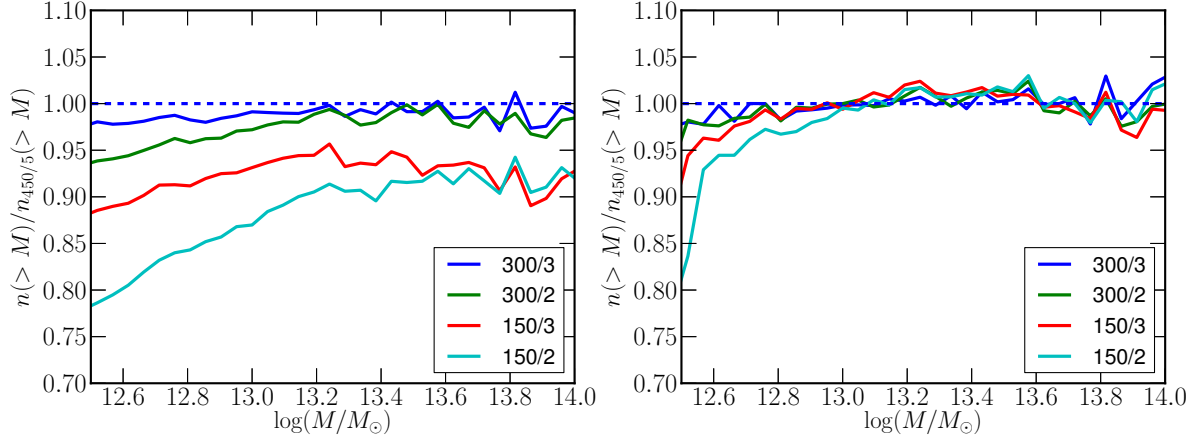

Figure 5. Comparison of cumulative mass functions in different simulations taking the 450/5 simulation as a reference. Lines, from top to bottom, correspond to the time stepping choices, 300/3 (blue), 300/2 (green), 150/3 (red), and 150/2 (cyan) respectively. The left panel shows the cumulative mass functions for unadjusted masses (as described in the text), while the right panel shows the post-correction results. A simple mass recalibration allows one to successfully recover the mass functions, even in the extreme case of the 150/2 simulation, for which the original result differed by more than 10% (on all mass scales).

We next compute the halo-matter cross power spectra between halo and matter density fields in both real and redshift space, as shown in Figure **??**. This figure shows the ratio $P_{hm}/P_{hm,450/5}$ at $z = 0.15$, where $P_{hm,450/5}$ is the cross power spectrum for the 450/5 simulation and P_{hm} is the cross power spectrum for other time steps. For the dark matter density field, we use the output of the 450/5 simulation for all the halo samples. Note that the dark matter density fields are in real-space for both cases. In this way, the ratio $P_{hm}/P_{hm,450/5}$ in real-space is equivalent to the ratio of halo bias between the 450/5 simulation and the simulations with other time-steps. To select halos, we apply the soft-mass cut method using the probability given by

$$\langle N_{halo}(M) \rangle = \frac{1}{2} \text{erfc} \left(\frac{\log(\mathrm{M_{cut}}/M)}{\sqrt{2}\sigma} \right), \tag{3.2}$$

where we set $\mathrm{M_{cut}} = 10^{13.0} [\mathrm{M_\odot}]$ and $\sigma = 0.5$. This probability has a similar form to the HOD technique so that the probability gradually becomes one as halo mass increases. We use this method to avoid noise from halos scattering across sharp halo mass boundaries. The errors calculated here are not due to sample variance as we generate 10 samples from one full sample with the soft-mass cut method. The results show that as the time stepping is coarsened, the ratio of the cross power spectra increases, especially in redshift-space, where we observe large deviations from unity on small scales for the 150/2 and 150/3 simulations. This is due to the overall smaller halo velocities for those simulations, as shown in Figure **??**. For the simulations with the 300 global time steps, overall agreement with the 450/5 simulation is almost at the 1% level on any scale in both real-space and redshift-space. Based on these convergence tests, we conclude that the 300/2 option meets the error requirements.
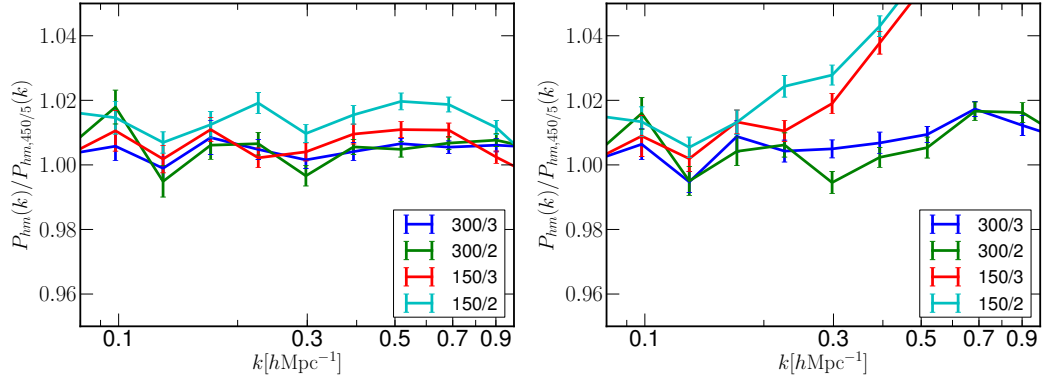
Figure 6. Ratio of halo-matter cross power spectra as a function of time steps with respect to the 450/5 simulation at $z = 0.15$. We use the real-space halo density field for the left panel and the redshift-space halo density field for the right panel; the dark matter density fields used here are in real-space for both cases. The left panel shows that agreements with the 450/5 simulation are all within 2%. In the right panel, the large discrepancy of the cross power spectra for the simulations with 150 global steps on small scales is mainly due to the systematically small velocities shown in Figure **??**. Note that the halos are selected based on the soft mass-cut method with $M_{cut} = 13.0$ and $\sigma = 0.5$.

4 Constructing Light Cones

Once the simulations are run at the chosen time-stepping settings, the next step is to construct light-cone outputs. Here, we build light cones from snapshots whose redshift range is from $z = 0.8$ to $z = 0.15$, with a constant redshift separation of $\Delta z = 0.1$. The light cone is constructed using spherical shells, each shell is centered at the redshift of each snapshot, and has a redshift width of 0.1. In each shell, we displace the halo positions by using their peculiar velocities in order to shift to light cone positions:

$$\vec{x}|_{z=z_{pos}} = \vec{x}|_{z=z_{snap}} + \vec{v}_{pec}|_{z=z_{snap}}\Delta t, \tag{4.1}$$

where z_{snap} is the redshift of the snapshot, z_{pos} is the redshift corresponding to its radial position, $\vec{v}_{pec}$ is its peculiar velocity, and Δt is the time elapsed between z_{snap} and z_{pos}. For the case of a halo crossing its boundary of the shell, we choose the halo whose distance from the boundary is closer before shifting.

To evaluate how shifting affects a spatial distribution of halos, we compare the distances for the halos at different redshift before and after shifting their positions. For the comparison, we use the halos which exist at both redshifts by matching halo particle profiles, which is the same method described in Section 3.1. Figure **??** is the histograms of distances for the matched halos at $z = 0.25$ and $z = 0.15$ before and after shifting. After shifting halos, we see that the mean distance between corresponding halos decreases from $0.4h^{-1}$Mpc to $0.1h^{-1}$Mpc and the standard deviation shrinks from $0.2h^{-1}$Mpc to $0.1h^{-1}$Mpc. This result holds at all redshifts examined.
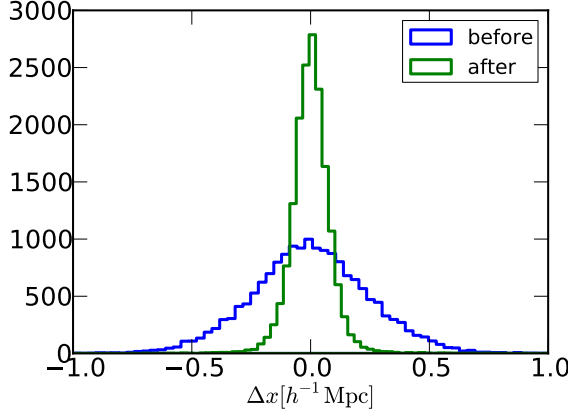
Figure 7. The histogram shown in blue is that of the distances between the position of the halos at $z = 0.25$ and where they have moved to in the simulation at $z = 0.15$. The histogram shown in green is that of the distances between the positions of the halos at $z = 0.15$, and the positions that would be predicted by shifting the positions from the $z = 0.25$ simulation assuming the peculiar velocity was constant between the snapshots (described in Eq. **??**). The plot shows that the distances between the halos at different redshifts become smaller after the shifting.

As an additional check, we compare the affect on halo bias due to shifting. Figure **??** shows the ratios of the halo matter cross power spectra to an auto matter power spectrum at $z = 0.25$. The plot shows that shifting halos from $z = 0.15$ to $z = 0.25$ brings down the halo bias to the one at $z = 0.25$ (an analogous test is shown for redshifts $z = 0.7$ and $z = 0.8$). The agreement between the original power spectrum at $z = 0.25$ and the shifted power spectrum is 99.8% up to $k = 1h\mathrm{Mpc}^{-1}$. This demonstrates that the spatial distribution of the halos is statistically correct across the scales of interest.
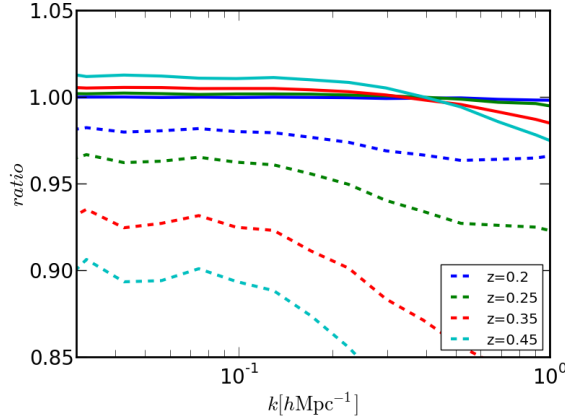

Figure 8. In this figure, we use the halo matter cross power spectra at $z = 0.25$ and $z = 0.7$ as a denominator. The dashed lines show the ratio with the cross power spectra at $z = 0.15$ and $z = 0.8$ respectively before shifting, and the solid lines are the ratio after shifting halo positions. It indicates that shifting the positions of halos from one redshift to the another preserves the distribution of halos statistically.

A parameter when building light cones by stitching static snapshots together is how large Δz can be between various snapshots. Figure **??** test this in both real and redshift space; in redshift space, we assume the velocity of the object is unchanged between the snapshots. We see that the agreement in real space is within 1% even for the case of shifting for $\Delta z = 0.25$, while the discrepancy increases more rapidly for larger Δz in redshift space. In order to understand the cause of rapid discrepancy of

the power spectra in redshift-space, we further investigate the distribution of velocity differences at different redshifts shown in Figure **??**. We compare original velocities computed from the simulations in the right panel, while we multiply those velocity by the expansion factor $a(z)$ in the left panel. By scaling with the expansion factor, the velocity differences at different redshifts become smaller. Figure **??** shows the power spectra recomputed with the velocity multiplied by the ratio of $a(z)/a(z = 0.15)$, where z is the redshift of the simulation. The clustering in redshift-space is improved significantly that the overall agreement becomes within 1% on $k < 1[h\mathrm{Mpc}^{-1}]$.

NOTE: velocity scaling with scale factor ratio needs to be justified –
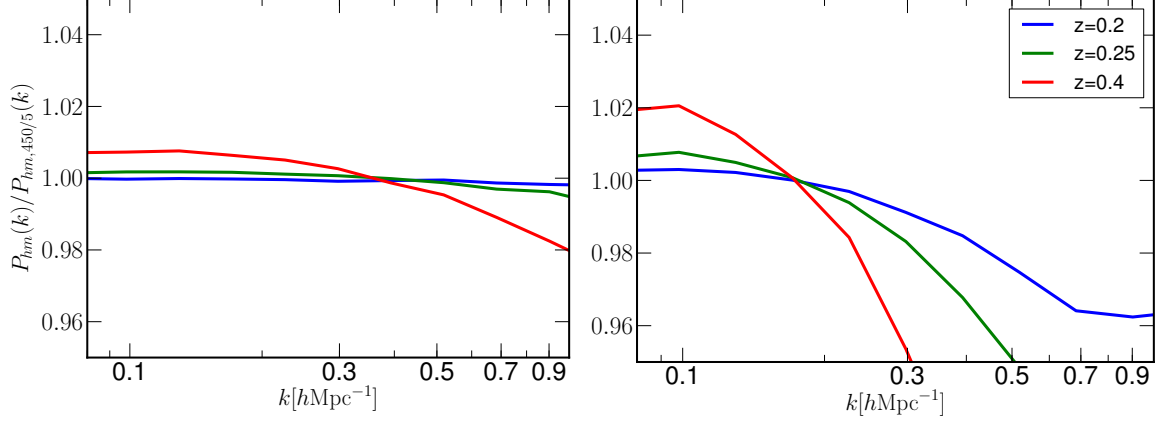
Figure 9. Ratio of halo matter cross power spectra in real space [left] and in redshift space [right] after shifting the position of the halos from the redshift labeled in the plots to $z = 0.15$. The denominator is the cross power spectra at $z = 0.15$, where we use the halo density field in real space and redshift space respectively. For all cases, we use the DM density field in real space at $z = 0.15$.
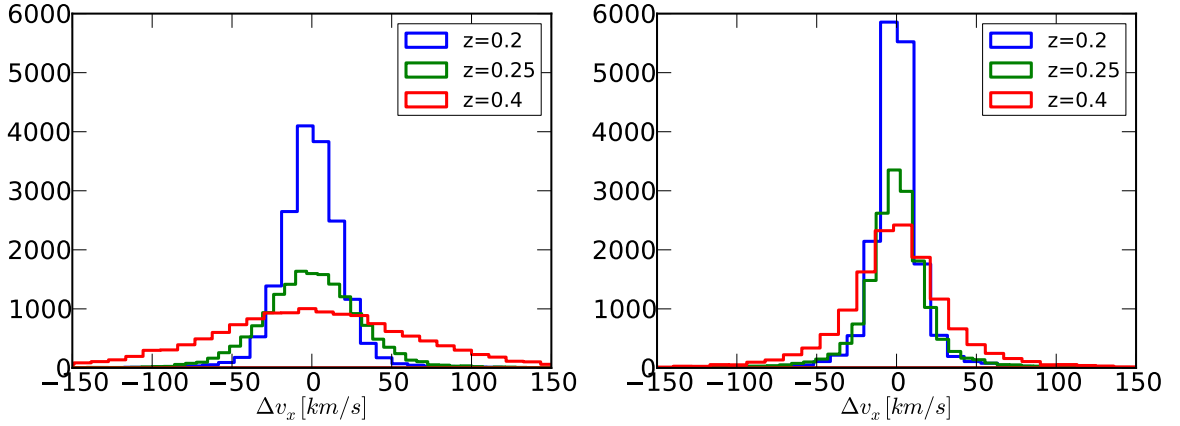

Figure 10. Comparisons of the velocities of halos matched across simulations at different redshifts to the one at $z = 0.15$. From left to right, we compare original halo velocities and the velocities multiplied by the expansion factor $a(z)$. As shown, the scatter in the velocity differences decreases in the right panel. This indicates that the change in velocities at different redshifts is largely affected by the expansion of the Universe.

5 BOSS Mock Catalogs

As a concrete implementation of the approach discussed above, we construct catalogs designed to mock BOSS galaxy samples. BOSS ([**?**]), part of the SDSS-III project ([**?**]), is a spectroscopic
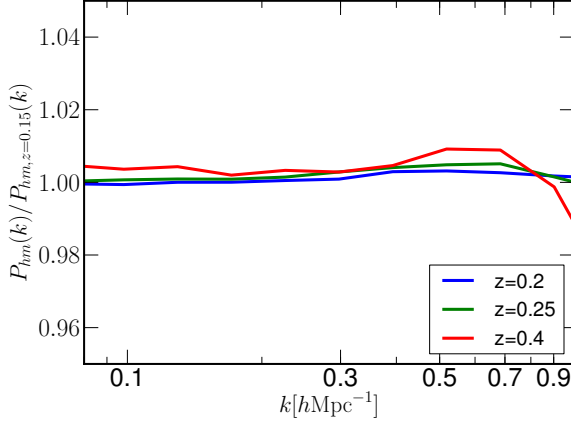
Figure 11. Ratio of halo matter cross power spectra in redshift space as shown in Figure **??**. The only difference is that here we use the velocity field multiplied by the ratio of the expansion factor $a(z)/a(z = 0.15)$ (where z is the redshift shown in the figure) to compute the halo positions in redshift-space. The denominator is the cross power spectra at $z = 0.15$, where we use the halo density field in redshift space. For all cases, we use the DM density field in real space at $z = 0.15$.

survey that aims to make percent level distance measurements using the baryon acoustic oscillation technique. The low redshift ($z < 0.7$) distance measurements use two galaxy samples : the LOWZ ($z < 0.45$) and CMASS ($z < 0.7$) samples ([**? ?**]). We focus on the CMASS sample below; however, the same halo catalogs are useful for the LOWZ sample as well.

We choose a simulation volume large enough to build a full-sky mock BOSS catalog. Since the CMASS sample extends to $z \sim 0.7$, we choose a simulation side of $4000h^{-1}$Mpc, corresponding to a comoving distance to $z \sim 0.8$ from the center of the box; Fig. **??** shows the BOSS CMASS redshift distribution as a function of redshift and comoving distance (assuming our fiducial cosmology). Our simulations are run with 4000^3 particles, corresponding to a particle mass of 10^{11}M$_\odot$. The characteristic halo mass for BOSS galaxies corresponds to $10^{13}M_\odot$, which we resolve with 100 particles. We keep all halos down to 40 particles corresponding to a halo mass of $10^{12.6}$M$_\odot$. The simulations are started at $z = 200$ with Zel'dovich initial conditions and are stopped at $z = 0.15$ with simulation outputs every $\Delta z = 0.05$. At each of these steps, we store XXX. NOTE: complete final sentence -¿ This is for Salman and Katrin to fill the details.

The BOSS angular geometry is split into two regions : one in the North Galactic Cap and one in the South Galactic Cap (Figure **??**). Since we generate full-sky mocks, it is straightforward to embed two full non-overlapping BOSS surveys in a single mock realization (Figure **??**). We cut out a first BOSS volume with $\vec{x}_{old}$ and then define a new coordinate system $\vec{x}_{new}$ such that $\vec{x}_{new} = R\vec{x}_{old}$, where R is the Euler rotation matrix for Figure **??**:

$$R = \begin{pmatrix} 0.088 & 0.096 & 0.991 \\ 0.219 & -0.973 & 0.075 \\ 0.972 & 0.211 & -0.107 \end{pmatrix}.$$

5.1 Building the Galaxy Catalog

To generate the galaxy mock catalogs, we proceed in two steps, 1) populate halos with galaxies using an HOD approach, 2) assign positions and velocities to the galaxies assuming an NFW profile [**?**]. The HOD functional form (based on a number of free parameters, 5 in our case) provides probabilities for the number of central and satellite galaxies based on the masses of halos that host those galaxies. A halo hosts a central galaxy with probability $N_{cen}(M)$ and a number of satellite galaxies given by a Poisson distribution with mean $N_{sat}(M)$:
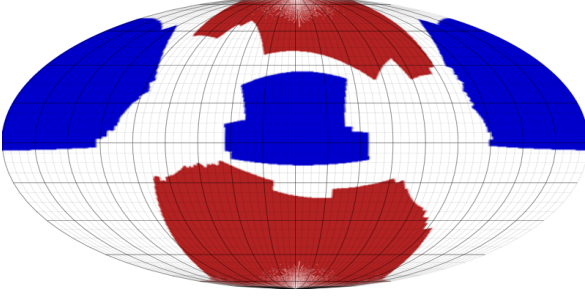
Figure 12. Fitting two non-overlapping BOSS volumes into the same simulation box. The blue region is the BOSS survey footprint in equatorial coordinates, while the red region is the same region rotated using the rotation matrix given in the text.

$$N_{cen}(M) = \frac{1}{2}\text{erfc}\left[\frac{\ln(M_{cut}/M)}{\sqrt{2}\sigma}\right], \tag{5.1}$$

and

$$N_{sat}(M) = N_{cen}(M)\left(\frac{M - \kappa M_{cut}}{M_1}\right)^\alpha, \tag{5.2}$$

where M_{cut}, M_1, σ, κ, and α are free parameters and M is the halo mass. We assume that $N_{sat}(M)$ is zero when $M < \kappa M_{cut}$ and halos do not host satellite galaxies without a central galaxy [**?**]. The total number of galaxies hosted by each halo is a sum of the number of central and satellite galaxies. Equations **??** and **??** are not the only possible functional form for the HOD, and it is trivial to change this. However, these forms are known to successfully reproduce the clustering of the BOSS galaxies [**?**] and are therefore a convenient choice.

Central galaxies are given a velocity equal to the halo velocity; satellite galaxies are distributed around them with a spherically symmetric NFW profile specified by:

$$\rho(r) = \frac{4\rho_s}{\frac{cr}{R_{vir}}(1 + \frac{cr}{R_{vir}})^2}, \tag{5.3}$$

where ρ_s is the density at the characteristic scale $r_s = R_{vir}/c$, R_{vir} is the virial radius for the halo and c determines how centrally concentrated the profile is. R_{vir} is computed from $M = \frac{4\pi}{3}R_{vir}^3\rho_{crit}\Delta_h$, where $\Delta_h = (18\pi^2 + 82(\Omega_m - 1) - 39(\Omega_m - 1)^2)/\Omega_m$ and $\rho_{crit} = \frac{3c^2 H_0^2}{8\pi G}$ (c is the speed of light here). We use a cosmic emulator [**?**] to generate a table of concentration-mass relation for halos at each redshift with the given cosmology.

The velocities of the satellite galaxies are the sum of their host halo velocity and a random virial component. This random component is given by

$$<v_x^2> = <v_y^2> = <v_z^2> = \frac{1}{3}\frac{GM}{R_{vir}}. \tag{5.4}$$

We draw a Gaussian distribution with zero mean and variance in Eq. **??** to give each component of an internal velocity for the satellite galaxies. Here, we assume that satellite galaxies are randomly moving inside the host halos.

We generate galaxy mocks from the static snapshots at $z = 0.55$. In Figure **??**, we compare the correlations function $\xi(s)$ with the one in [**?**], where s is the separation in redshift-space. Here, we use the following HOD parameters, $M_{cut} = 12.9$, , $\alpha = 1.013$, $\kappa = 1.0$, $\sigma = 0.85$.

We subsample to match the redshift selection function of Ref. [**?**]. Figure **??** shows before and after subsampling for BOSS CMASS North Galactic Cap.

NOTE: not clear at all what is being done here; what do the dashed lines in Fig. 13 mean? Should we even show Fig. 13?
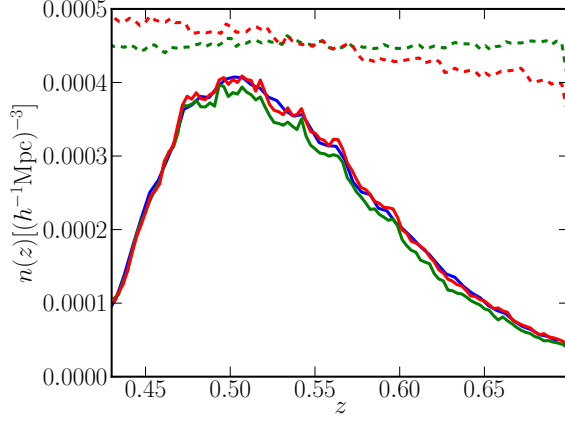
Figure 13. A comparison of galaxy number densities before fitting to DR11 (dashed lines) and after (solid lines). The blue solid line is $n(z)$ from DR11 (North) in Ref. [**?**]. The green and red lines are from the mocks at $z = 0.55$ and the lightcone output respectively. The HOD parameters used to generate the mock catalogs can be found in text.
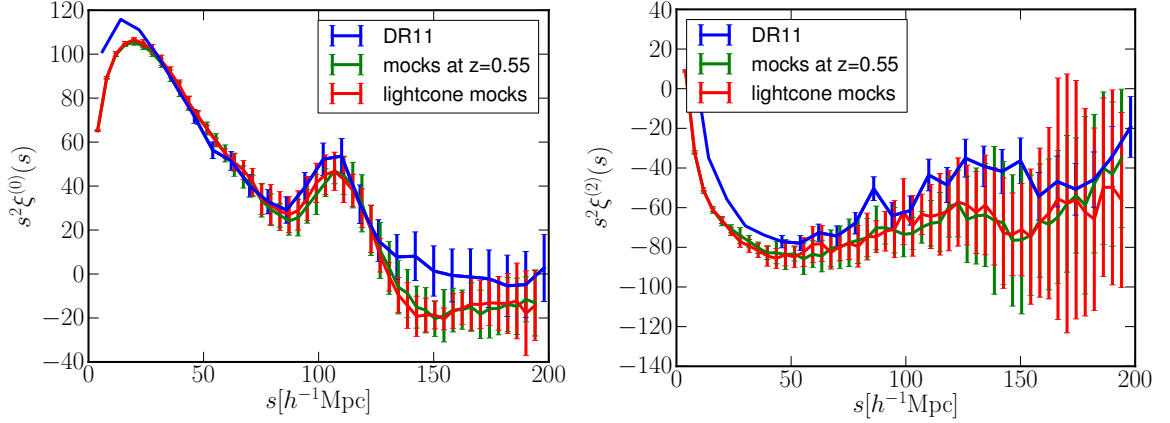

Figure 14. Correlation function monopoles $\xi^{(0)}(s)$ (left) and quadrupoles $\xi^{(2)}(s)$ (right) of the mocks (green) and DR11 in Ref. [**?**] (blue) at $z = 0.55$. The HOD parameters used to generate the mock catalogs can be found in text.

The correlation function computed from our sample mocks agrees with the correlation function in Ref. [**?**] well on the scale between $30h^{-1}$Mpc and $80h^{-1}$Mpc shown in Figure **??**. We compute χ^2 for monopoles and quadrupoles from the simulation at $z = 0.55$ and the light cone output. We obtain $\chi^2 = 23.4$ for the simulation at $z = 0.55$ and $\chi^2 = 25.0$ for the light cone output. The degree of freedom here is 14 where $s \in [30h^{-1}\text{Mpc}, 78h^{-1}\text{Mpc}]$.

NOTE: better and more complete discussion of the results is needed here; how well do our mock results compare with those obtained by other people? why is the chi^2 a relevant test here?

NOTE: not clear what the point of this figure is

NOTE: need a better discussion of these results in the text

6 Discussion

Precision required for current and future galaxy spectroscopic surveys to test the expansion and structure formation histories of the Universe requires an accurate understanding of systematic effects. In this paper we have presented a quantitative study of the impact of time step sizes on the halo

and matter density fields. Our code has two adjustable time stepping parameters - a global time step and a number of sub-cycles (responsible for a particle-particle interactions) to track that particle trajectories on small scales. We consider cases where we increase the length of each time step by factors of 1.5 and 3 respectively, as well as reducing the number of sub-cycles. Our fiducial choice is to use using 300 global time steps corresponding to $\Delta a(z) = 0.003$ and 2 sub-cycles (increasing the length of the global time step by a factor of 1.5 and that of the sub-cycles by a factor of 2.5), resulting in a reduction of the simulation run time by 4 times less. We keep the mass resolution constant; the results here are based on a particle mass of $6.86 \times 10^{10} h\mathrm{M}_\odot$. We summarize the key results below:

(a) The halo masses tend to be underestimated in these cases, as one might expect because reducing the number of time steps produces halos with less substructure and a more diffuse distribution of mass. However, this trend may be calibrated with smaller simulations and corrected, recovering the halo masses to 98%. The halo mass function is correctly recovered fully for masses above $10^{12.7} h^{-1}\mathrm{M}_\odot$ corresponding to 100 particles. Note that we run the halo finder with identical parameters as in the full resolution runs. It may however be possible to get similar results by changing the parameters of the halo finder, as was done in [?].

(b) The halo positions and velocities are recovered with a scatter of $0.08[h^{-1}\mathrm{Mpc}]$ and $12.8[\mathrm{km/s}]$ respectively for the simulation of our fiducial choice.

(c) The clustering of these halos is correctly recovered to better than 1% on scales below $k < 1[h\mathrm{Mpc}^{-1}]$ in real-space and $k < 0.5[h\mathrm{Mpc}^{-1}]$.

(d) We find that the number of sub-cycles makes almost no difference to any of our final results.

We also consider the redshift sampling required to construct light cone outputs. We first compare the distances for the halos at different redshifts before and after shifting their positions from one redshift to the another. Moving halos over a $\Delta z = 0.1$ interval correctly reduces the standard deviation of those distances from $0.25[h^{-1}\mathrm{Mpc}]$ to $0.09[h^{-1}\mathrm{Mpc}]$. Moreover, the power spectra are correctly recovered to better than 1% for $k < 0.5[h\mathrm{Mpc}^{-1}]$ for $\Delta z = 0.25$. This worsens in redshift space to 2% up to $k < 0.2[h\mathrm{Mpc}^{-1}]$. The agreement is, however, improved to 1% for $k < 1[h\mathrm{Mpc}^{-1}]$ by using the velocity scaled by the relative scale factor between the snapshot and the true redshift. Our fiducial choice to construct light cone outputs is $\Delta z = 0.05$.

This work is a natural extension of the approaches described in [? ? ? ? ?]. The primary goal for those papers was to generate the large numbers of simulations required for estimating covariance matrices. We quantify, in detail, the impact of size of the time step on large scale observables; our suite of simulations are better designed for testing for systematic errors in theory and analysis techniques. As a proof of principle, we present a set of eight full BOSS (both North and South Galactic caps simultaneously) simulations. The time savings presented in this paper allowed to extend this to 50 simulations, across a range of cosmologies. These results from these will be presented in future publications.

Acknowledgement